Heliyon 10 (2024) e29750

Contents lists available at ScienceDirect

Heliyon

journal homepage: www.cell.com/heliyon

Research article

Corrosive effect on saturated pool boiling heat transfer characteristics of metallic surfaces with hierarchical micro/nano structures

Wei Xu [a], Longchang Tang [b], Ningkang Zhao [a], Kun Ouyang [b], Xiaoqiang He [c], Xiaojing Liu [b,*]

[a] College of Smart Energy, Shanghai Jiao Tong University, Shanghai, 200240, China
[b] School of Nuclear Science and Engineering, Shanghai Jiao Tong University, Shanghai, 200240, China
[c] Science and Technology on Reactor System Design Technology Laboratory, Nuclear Power Institute of China, Chengdu, 610041, China

ARTICLE INFO

Keywords:
Corrosive effect
Hierarchical micro/nano structure
Pool boiling
Critical heat flux
Bubble dynamics

ABSTRACT

Surface modification is of critical interest to enhance boiling heat transfer in terms of heat transfer coefficient or critical heat flux (CHF), which is significantly affected by distinct surface morphology and wettability and it can improve the efficiency and safety of equipment. Furthermore, actual service environment may cause severe corrosion to the processed structured surfaces while its consequence on boiling heat transfer is still obscure. In this article, comprehensive researches are conducted to unravel corrosive effect on metallic samples made of stainless steel (SS) and Inconel materials with microstructures. Different constructions (i.e., microgroove, microcavity and micropillar array) and characteristic dimensions (~20, 50 μm) of microstructure, various duration time (up to 300 days) and pH values (~7.0–8.5) of corrosive environment are compared thoroughly. Conclusions can be drawn that not all microstructures can enhance pool boiling heat transfer characteristics, especially in terms of CHF values. More importantly, CHF value of SS microgroove sample firstly increases from 60.94 to 94.09 $W{\cdot}cm^{-2}$ in 50 days, then decreases to 47.77 $W{\cdot}cm^{-2}$ in 300 days, which can be attributed to competition result between formation of hierarchical micro/nano structure with enhancing wicking capability and chemistry condition with increasing contact angle. In addition, distinct bubble dynamics during pool boiling is also analyzed. The insights obtained from this article can be used to guide surface modification method and to reveal evolvement rule of engineered metallic surface in highly corrosive and harsh boiling heating transfer environment.

1. Introduction

Boiling heat transfer is a ubiquitous phenomenon in daily life and industrial scenes, which can utilize the latent heat of coolant during phase change process to dissipate enormous generated heat within equipment. Due to the intrinsic feature of efficient heat transfer capability [1], boiling heat transfer is widely used in water desalination [2], chemical processing [3], thermal management of electronics [4,5] and power generation [6]. Usually, boiling performance can be characterized by two parameters: heat transfer

* Corresponding author.
E-mail address: xiaojingliu@sjtu.edu.cn (X. Liu).

https://doi.org/10.1016/j.heliyon.2024.e29750
Received 16 November 2023; Received in revised form 12 April 2024; Accepted 15 April 2024
Available online 16 April 2024

coefficient (HTC) and critical heat flux (CHF) [7]. The HTC in saturated pool boiling can be defined as the ratio between heat flux and wall superheat degree. The higher HTC is, the lower superheat (i.e., lower wall temperature) can be obtained at a specified heat flux value, which can improve the operation efficiency and economy of equipment. In addition, CHF is regarded as the upper limit of nucleate boiling regime so that the safety margin of equipment can be significantly boosted with a higher CHF value. Especially in a nuclear power plant (NPP), the occurrence of CHF can lead to a drastic increase of cladding temperature, which is vital to the integrity of fuel cladding, and catastrophic melting down may occur as a severe consequence [8].

Surface modification via engineered structures has been a topic of general interest in order to enhance boiling heat transfer [9–11]. The properties of boiling surface (such as morphology, roughness, wettability and so on) can significantly alter bubble dynamics and corresponding heat transfer characteristics. For instance, surface with microcavity (MC) [12] array can improve the HTC value by promoting vapor bubble nucleation [13]. While surfaces with microgroove (MG) [14] and micropillar (MP) [15] array usually have a higher CHF value resulted from the contact line augmentation and capillary-fed rewetting [16]. Besides, CHF value is dependent on surface roughness noticeably: Kim et al. [17] found that CHF value at the roughest surface (Ra = 2.36 μm), i.e., 162.5 $W{\cdot}cm^{-2}$, is approximately twice as much as that at the smoothest surface (Ra = 0.041 μm). In addition to microstructure, surface wettability can also affect boiling heat transfer performance: the nucleation sites on hydrophobic surface are easy to be activated, and possibly enhance HTC but result in a lower CHF; as a contrast, the hydrophilic surface can delay the formation of continuous vapor blanket so that a higher CHF value can be obtained [18,19].

As aforementioned, surface modification is beneficial to the enhancement of boiling heat transfer of large-scale equipment, but is threatened by the corrosive environment of high temperature and pressure in NPP. Son et al. [20] conducted pool boiling experiments to evaluate the effect of oxidation of reactor pressure vessel (RPV) material, and the CHF value of oxidized steel alloy decreased because of oxide layer properties. Wang et al. [21] found that more oxidized surface can reach to higher CHF value, which can be attributed to combined effect of increasing wettability and decreasing nucleation site density. In addition, the wettability of modified surface can also be altered by passive atmospheric adsorption of hydrophobic volatile organic compounds (VOCs) [22], which eventually makes it more sophisticated under actual corrosive situation. Therefore, the mechanism of corrosive effect on boiling heat transfer has not been researched thoroughly.

In this article, metallic samples made of stainless steel (SS) and Inconel materials are adopted for further comparison, which are commonly utilized in NPP. Three typical microstructures, i.e., MG, MC and MP array are fabricated by laser processing through ablation and melting of base material using pulse fluences [23]. High-pressure corrosion experiments with different duration time and water chemistry conditions are conducted comprehensively, which are similar with that in the primary loop of pressurized water reactor. Subsequently, both the microscopic characterization and macroscopic behavior are combined to unravel complex corrosive

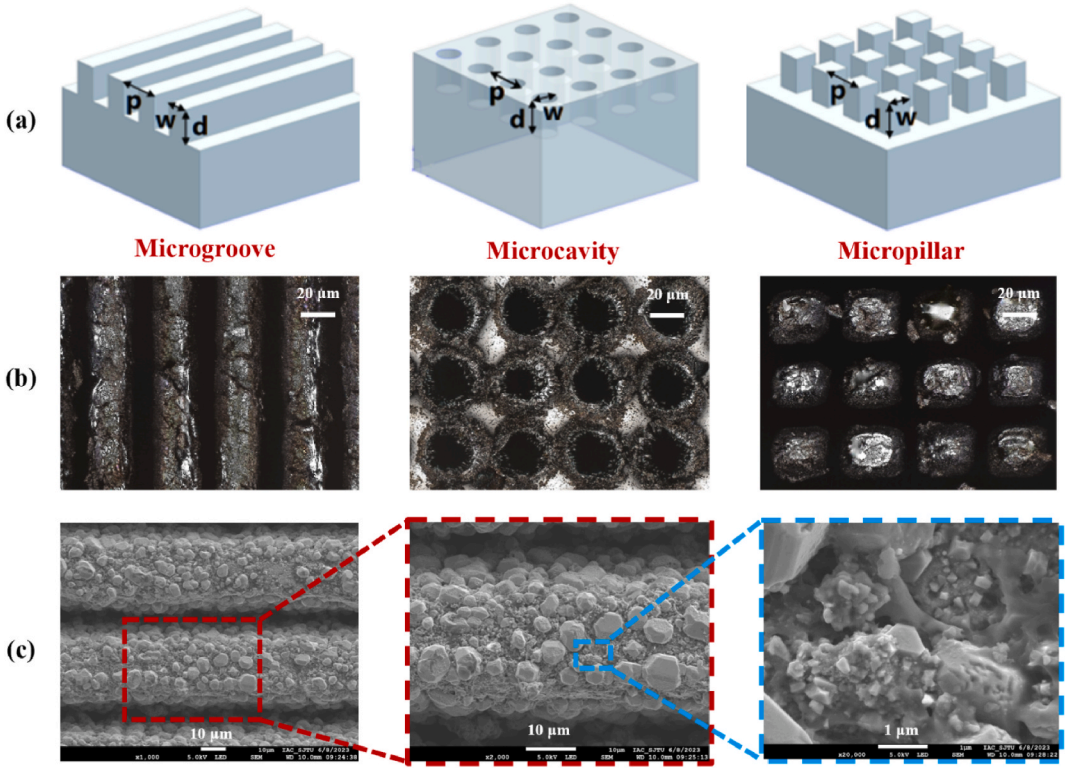

Fig. 1. (a) 3-D schematic diagram (not to scale) and (b) LSCM images of MG, MC and MP array samples, (c) SEM images about hierarchical micro/nano structure of MG array sample corroded for 100 days.

effect on boiling heat transfer performance of metallic surface with structures. The research results can be utilized for optimization of boiling heat transfer surface design in the nuclear reactor.

2. Experimental investigation

2.1. Sample preparation

Two specific metallic materials, i.e., SS (wt.%: Fe 85.96 %, Cr 13.00 %, Si 0.77 %) and Inconel (wt.%: Ni 55.25 %, Cr 33.21 %, Fe 8.63 %, C 1.57 %), measured by Energy Disperse Spectroscopy (EDS, JSM-7800F JEOL), are selected for sample preparation. Firstly, these plate-type samples are grinded with various abrasive papers (600#, 1200#, 2000# in sequence) and polished with Al2O3 particles and cloths. After that, all these samples are rinsed with ethanol (5 min) and deionized water (2 min), respectively. Considering that heat conductivities of these metals are relatively low (<20 W/m·°C) [24], the thickness of plate-type samples are designed as 0.8 mm to minimize the operating temperatures of pool boiling test facility, especially under high heat flux condition.

Typical MG, MC and MP array surfaces are fabricated by laser processing (Deli Laser Solutions, Jiangyin) to investigate the morphology effect on pool boiling heat transfer. The sample is placed on a computer-controlled 3D translation stage, the microstructure is fabricated through the laser beam path set up in advance and the number of pulses is controlled by adjusting translation speed of samples [18]. As shown in Fig. 1 (a) (dimensions are not to scale), the width of MG, diameter of MC, side length of MP (labeled as w) and pitch distance (labeled as p) all have equal design dimensions (~20, 50 μm), while depths (labeled as d) are nearly 1.5 times of that value. The processed texturing of structured surfaces can be observed obviously from laser scanning confocal microscopy (LSCM) images (Fig. 1, (b)). After that, all microstructure samples are placed in high-pressure autoclaves with different chemistry conditions. The detail of corrosion equipment and boundary conditions are depicted in Sec. 2.2.1. Fig. 1 (c) shows the scanning electron microscope (SEM) images (JSM-7800F JEOL) of MG-20 sample corroded for 100 days. Massive oxide particles ranging from nanometer to micron are formed and stacked on the MG structure, its original morphology has been altered to hierarchical micro/nano structure as a result. More SEM details can be found in Fig. S5 with distinct surface morphology of microstructures.

2.2. Experimental apparatus

2.2.1. Construction of corrosion test facility

In view of high temperature/pressure and water chemistry environment in the primary loop of nuclear reactor, the corrosive behavior of metal materials (i.e., SS and Inconel alloy) are definitely distinct, which can impact the boiling heat transfer characteristics significantly. In this article, high pressure autoclaves with various water chemistry are utilized to simulate typical nuclear reactor environment, and the details of boundary conditions are listed in Table 1. It is worth mentioning that the boundary conditions are not all the same with nuclear power plant, which are more severe (higher pH value) to accelerate the corrosion speed.

As depicted in Fig. 2, the autoclaves are heated by a ceramic heating ring, and both of them are surrounded by gray-colored thermal insulation. The ceramic heating ring is connected to a temperature controller and a constant value of 350 °C can be maintained, which is monitored by the TC inserted in the middle site. Corresponding saturated pressure, nearly 10.0 MPa can also be hold for different corrosion time. The boric acid and lithium hydroxide solution are mixed quantitatively so that three different pH values conditions (~7.0, 7.5 and 8.5 in high temperature) can be compared to figure out corrosive effect on pool boiling of microstructure samples.

2.2.2. Construction of pool boiling test facility

A test facility is established to conduct saturated pool boiling experiment of different microstructures samples, which mainly consists of the pool boiling chamber, heating section, high-speed camera (Qianyanlang X213), data acquisition system (National Instruments, NI-9128) and so on, as depicted in Fig. 3 (a). The dimensions of pool boiling chamber are 30.0 cm, 30.0 cm and 25.0 cm in length, width and height, respectively. Glass windows are installed to obtain the high-speed filming results of bubble dynamics. In addition, two cartridge heaters with total heating power of 3.0 kW are horizontally placed to ensure saturation condition of deionized water in the chamber. It is necessary to mention that the water level can always be maintained higher than 80.0 mm, so that boiling characteristics will not be influenced by water level [25].

The design of heating section is illustrated in Fig. 3 (b), the plate-type sample is placed on the top side of copper heat conduction section and fixed by an insulation cover with screws. Heating rods are placed inside the copper section, which are connected to an adjustable DC power supply with a maximum heating power of 1.05 kW. Considering that the boiling surface area of test sample is nearly 20.0 × 20.0 mm (in Supplement S1, Fig. S1), which is considered to be sufficiently large if the Bond number (ratio between buoyancy and surface tension forces) is greater than 3.0 [26] and it is nearly 63.71 in this article. Besides, two layers of thermal insulation material are wrapped outside the copper heat conduction section to decrease heat loss as much as possible: the inner layer is

Table 1
Parameters of corrosive boundary conditions.

Autoclave No.	Temperature (°C)	Pressure (MPa)	pH	Boric Acid (ppm)	Lithium Hydroxide (ppm)
#1	310.0	~10.0	~7.0	1000	1.2
#2	310.0	~10.0	~7.5	1000	4
#3	310.0	~10.0	~8.5	1000	55

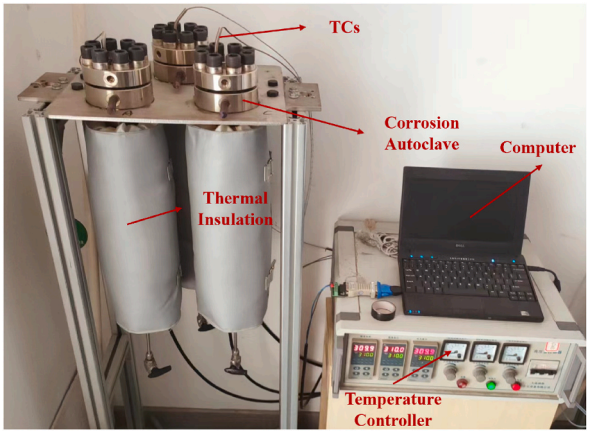

Fig. 2. Snapshot of corrosion test facility.

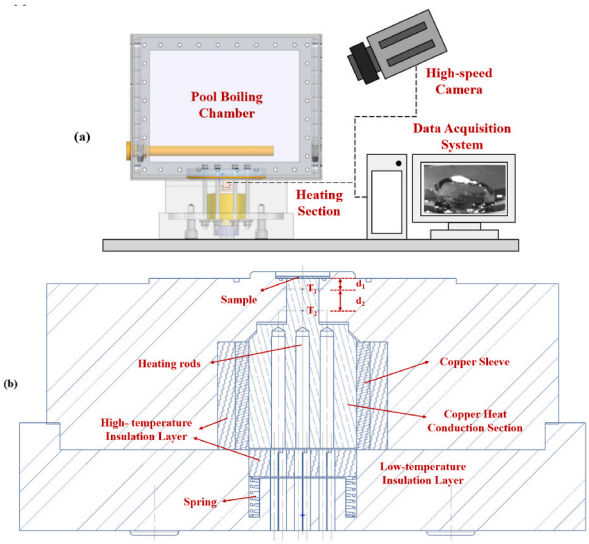

Fig. 3. (a) Schematic diagram of pool boiling test facility, (b) Cross-section diagram of heating section.

made of high-temperature resistant glass fiber sheet; the outer layer (polyetheretherketone, PEEK) has the advantages of good machinability and thermal insulation performance. Regarding the thermal expansion coefficient difference of copper and PEEK materials, it is difficult to maintain close contact between bottom side of test sample and top side of copper section during whole heating process, which is especially fatal to the indirect heating method adopted in this article. To solve this problem, a novel design combining a metal spring of suitable elastic coefficient and a copper sleeve is adopted in this article. Then the copper section can be lifted by spring to ensure close contact with the bottom side of test sample, and a relatively low friction (copper sleeve) also can be kept during heating process. During pool boiling, both visualization and measured thermocouples (TCs) results are recorded for contrastive analysis of difference cases. The procedures of saturated pool boiling are listed in Supplement S3 in detail.

2.3. Calculation methods

At the upper part (rectangular shape) of copper heat conduction section (Fig. 3 (b)), two K-type TCs are located vertically to measure the solid temperature. Considering that the copper heat conduction section is wrapped by two insulation layers except for the top side, hence the heat conduction from the lower copper section to upper test sample can be regarded as one-dimensional. Therewith, the value of steady heat flux q through test sample can be calculated by the recorded temperatures of TCs with Fourier's law

$$q = k_{Cu}\frac{T_2 - T_1}{d_2} \tag{1}$$

shown in Eq. (1):

Where k_{Cu} is thermal conductivity of copper and taken as 398 W/m·°C [27]. T_1 and T_2 are the measured temperatures of TCs and d_2 is the distance between them. Based on the calculated heat flux q, the value of surface temperature of test sample can be obtained by Eq. (2):

$$T_{surface} = T_1 - q\frac{d_1}{k_{Cu}} - q\frac{d_{grease}}{k_{grease}} - q\frac{d_{sample}}{k_{sample}} \tag{2}$$

where $T_{surface}$ is the surface temperature of test sample. d_1 is the distance between TC T_1 and top side of copper heat conduction section; d_{grease} and k_{grease} are thickness and conductivity of thermal grease, respectively, which is utilized between sample and copper section to minimize the contact heat resistance. It is worth mentioning that d_{grease} is difficult to measure directly, therefore an auxiliary setup (in Fig. S2) was adopted to evaluate the resistance of thermal grease. Combined with the values of heat flux and surface temperature (superheat degree), corresponding boiling HTC (h) can also be calculated as shown in Eq. (3):

$$h = \frac{q}{T_{surface} - T_{sat}} \tag{3}$$

where T_{sat} is the saturated temperature of atmospheric pressure.

2.4. Uncertainty analysis

The uncertainty of heat flux (including CHF) mainly comes from the measurement error of TC and dimension error of machining. Given that the maximum relative uncertainty of K-type thermocouple (OMEGA, TJ36-CASS) is 0.75 % and machining precision is approximately ±0.03 mm, then uncertainty of indirect measurements can be calculated with the error propagation formula [28] depicted in Eq. (4).

$$\frac{\delta F}{F} = \frac{1}{F}\sqrt{\sum_1^N \left(\frac{\partial F}{\partial X_i}\delta X_i\right)^2} \tag{4}$$

For the calculated heat flux q, it can be written as Eq. (5):

$$\frac{\delta q}{q} = \sqrt{\left(\frac{\delta T_2}{T_2 - T_1}\right)^2 + \left(\frac{\delta T_1}{T_2 - T_1}\right)^2 + \left(\frac{\delta d_2}{d_2}\right)^2} \tag{5}$$

For the boiling heat transfer coefficient h, the expressions of relative uncertainty are shown as Eq. (6):

$$\frac{\delta h}{h} = \sqrt{\left(\frac{\delta q}{q}\right)^2 + \left(\frac{\delta T_{surface}}{T_{surface} - T_{sat}}\right)^2} \tag{6}$$

Considering that the expressions of thermal resistance (d_{grease}/k_{grease}) and surface temperature of test sample are extraordinarily complex, which will not be listed here. Finally, the uncertainties of heat flux q, surface temperature of test sample $T_{surface}$ and heat

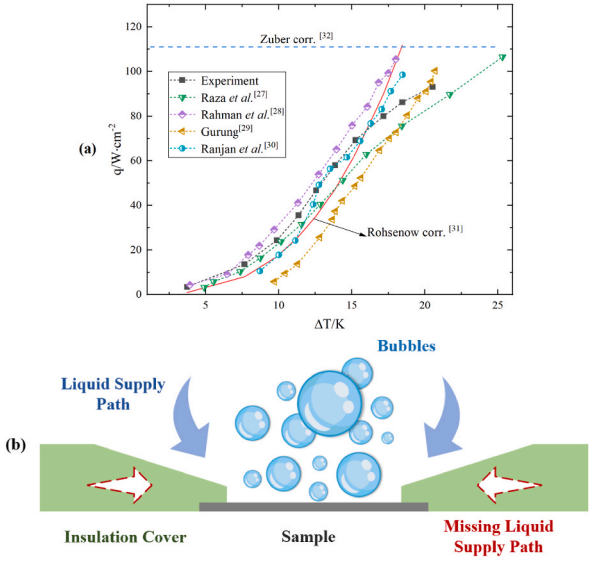

Fig. 4. (a) Comparison results of boiling curves with other researches, (b) Schematic diagram of missing liquid supply mechanism.

transfer coefficient h are 5.63 %, 1.57 % and 5.84 %, respectively.

3. Results and discussion

3.1. Validation of bare copper sample

Considering that saturated pool boiling characteristics are strongly dependent on heater material [29] and surface morphology, bare copper samples are prepared with same procedures to conduct pool boiling experiment in order to validate the applicability of test facility and accuracy of calculation method. It can be observed from Fig. 4 (a) that the obtained CHF value in this article (93.1 W·cm^{-2}) is located within the envelope of other researches (from 98.6 to 106.3 W·cm^{-2}) [30–33]. Furthermore, the profile of nucleate boiling regime is in accordance with Rohsenow correlation [34] (Eq. (7)):

$$\frac{c_{pl}\Delta T}{h_{fg}} = C_{sf}\left\{\frac{q}{\mu_l h_{fg}}\left[\frac{\sigma}{g(\rho_l-\rho_v)}\right]^{0.5}\right\}^{0.33}\mathrm{Pr}_l^n \tag{7}$$

where C_{sf} and n are empirical coefficients related to wall condition and liquid property, and the dimensions are taken as 0.0012 and 1, respectively, and corresponding root mean square error (RMSE) is only 14.4 %.

In addition, the upper limit (blue horizontal line) calculated by Zuber CHF model [35] derived from hydrodynamic instability is nearly 110.0 W·cm^{-2}. The reason why the obtained CHF value is lower than that of theoretical limit predicted by Zuber can be mainly attributed to the structure of insulation cover and test sample thickness. Given that the wedge-shaped insulation cover is located on top of test sample, the liquid supply path, especially in the horizontal direction (in Fig. 4 (b)), is disturbed during pool boiling. Besides, as proposed by Golobič I et al. [36] that 'asymptotic heater thickness, above which it does not significantly affect the CHF value, in the case of AISI 316 SS is equal to 845 μm, and this value is still a little thicker than that in our experiments (~800 μm). In summary, compared with other theoretical and experimental results of bare copper sample, the obtained boiling curve profile and CHF value in this article are both relatively reasonable. Next, the prepared SS and Inconel samples will be tested to reveal the effects of microstructures and corrosion.

3.2. Not all microstructures can enhance surface boiling heat transfer

Boiling heat transfer behaviors of uncorroded samples with various microstructures and characteristic dimensions are discussed in this section. The boiling curves of bare, MG-20, MC-20 and MP-20 SS samples are shown in Fig. 5 (a). Considering that the processed

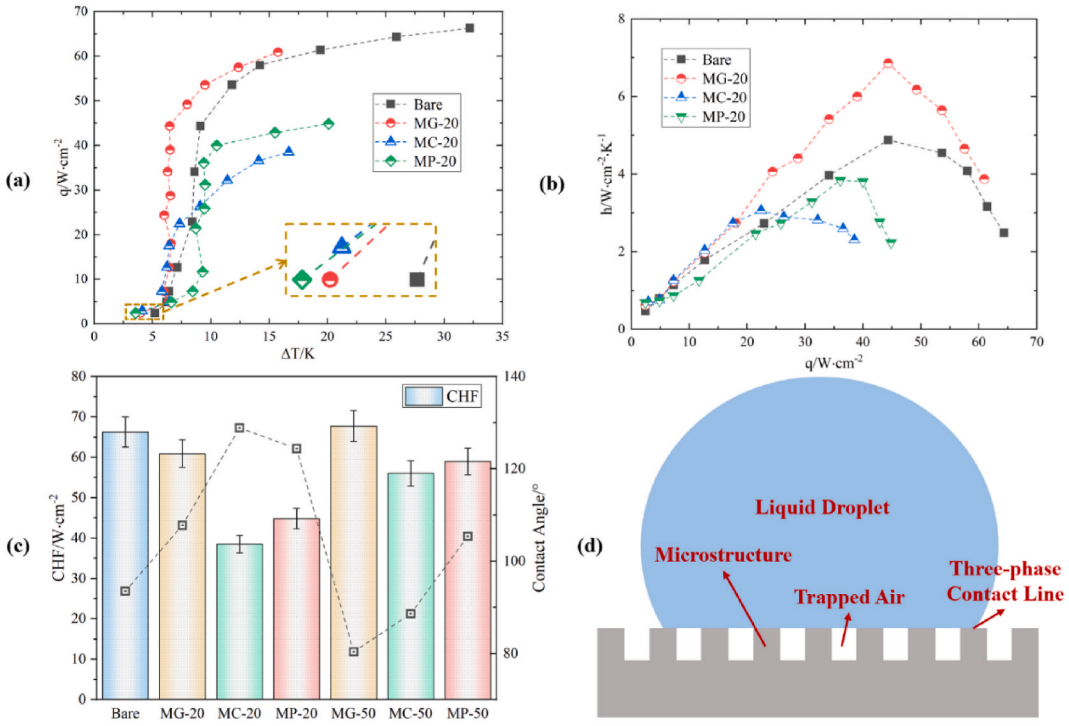

Fig. 5. (a) Boiling Curves and (b) HTC variation curves versus heat flux of bare, MG-20, MC-20 and MP-20 SS samples, (c) Relation between CHF and CA values of all SS samples, (d) Schematic diagram of Cassie-Baxter state on microstructure surface.

microstructures can be regarded as artificial nucleation sites, the features of onset of nucleate boiling (ONB) are altered. As shown in the inset of Fig. 5 (a), the bare sample has larger wall superheat value, which can be explained with Eq. (8) by combining the bubble Laplace pressure and Clausius-Clapeyron relation [37]:

$$\Delta T_{ONB} = \frac{2\sigma T_{sat}}{h_{fg}\rho_g R} \tag{8}$$

where R is microstructure radius of effective nucleation site. This equation reveals the inverse relation between wall superheat and microstructure radius, so that bare sample has a larger superheat resulted from the smaller radius of nucleation sites. Further, MG-20 sample has the largest CHF value among these microstructure samples, while all of them are lower than that of the bare sample. This seemingly abnormous result reveals that not all microstructures can enhance the boiling CHF value in certain conditions. It can be attributed to the fact that not only morphology, but also surface wettability can alter boiling heat transfer capability significantly. Fig. 5 (c) depicts the relationship between CHF and contact angle (CA, measured by DSA 100 KRüSS) values. It can be drawn that CHF value of bare, MG-20, MC-20 and MP-20 samples are inversely proportional to CA values, which ranges from 93.5° (bare) to 128.9° (MC-20) and details can be found in Table S1. The conclusion is also basically true among the MG-50, MC-50 and MP-50 samples. Kandlikar [38] proposed a CHF prediction model (Eq. (9)) that takes the receding angle into account:

$$q^{*} = h_{fg}\rho_v^{1/2}\frac{1+\cos\beta_r}{16}\left[\frac{2\sigma}{D_b} + (\rho_l - \rho_v)g\frac{D_b}{4}(1+\cos\beta_r)\right]^{0.5} \tag{9}$$

where β_r is the receding angle. This equation reveals that the CHF value is inversely proportional to the receding angle, and corresponding predicted values of uncorroded SS samples can also match the experimental CHF data well (less than 28 %, Fig. S4). Besides, the CHF values of microstructure samples with dimension 50 μm are larger than those with dimension 20 μm. This is mainly due to the easier downward liquid penetration (lower Laplace pressure) and smaller CA values, then the boiling crisis can be delayed with more lateral liquid supply underneath the bubble.

Fig. 5 (b) shows the variation tendency of HTC versus increasing heat flux. All the HTC curves increase firstly then decrease until CHF occurs, this situation is also encountered with other laser processed surfaces [38], which may be attributed to increasing thermal resistance of generated vapor film. Among those samples, even though MC-20 has the smallest CHF value during pool boiling, while it generally has the largest boiling HTC in the low heat flux region, which owes to massive nucleation sites [12] of microscale cavities. It can also be verified by visualization results (Fig. 6 (c)) that MC-20 sample has larger nucleation site density and smaller bubble departure diameter (≈ 1.8 mm). In high heat flux region, intensively generated vapor bubbles intend to coalesce with each other but

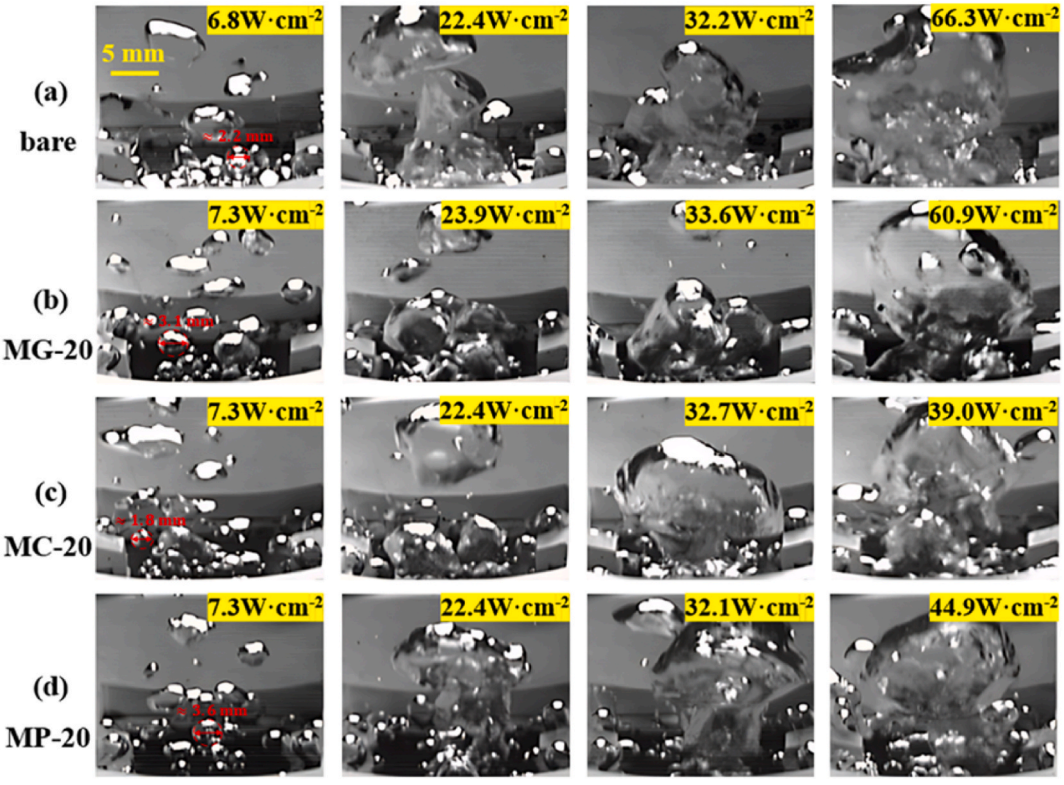

Fig. 6. Pool boiling visualization results of (a) bare, (b) MG-20, (c) MC-20, (d) MP-20 SS samples with different heat fluxes.

there are no interflows among nucleation cavities. In view of MG and MP samples, a larger CHF can be obtained with additional liquid supply and vapor escape pathways [39] to postpone the occurrence of boiling crisis. In addition, the difference of CHF values between MG and MP samples is probably related to the flow friction [40] with distinct surface morphology.

Fig. 5 (d) illustrates that a liquid droplet rests on the tips of microstructures, which is defined as Cassie-Baxter state [41]:

$$\mathrm{Cos}\,\theta_{C-B} = \varphi(1 + \mathrm{Cos}\,\theta_Y) - 1 \tag{10}$$

where φ is the ratio of microstructure area to projected area, θ_Y is the intrinsic CA of force balance at three-phase contact line and calculated by interfacial tensions. Based on measurement result in Fig. S3 (a), the intrinsic CA of bare SS sample can be regarded as 93.5°. Considering that the CA of air is 180°, hence the microstructure samples only can be more hydrophobic with the existence of trapped air. It is worth mentioning that the actual CA of microstructure samples does not match Eq. (10) exactly, and the realistic situation is more sophisticated that CA not only depends on surface morphology, but also chemistry condition.

In addition, the bubble dynamics also plays an essential role during nucleate boiling heat transfer process. Fig. 6 shows the visualization results of SS samples captured by a high-speed camera (500 fps) with different heat fluxes. In the first column (6.8–7.3 W·cm^{-2}), MP-20 sample (Fig. 6 (d)) has relatively larger bubble departure diameter (≈ 3.6 mm) and fewer nucleation sites than MC-20, which results in a lower HTC (Fig. 5 (b)). With the increasing heat flux, massive generated bubbles coalesce with each other, the liquid supply to heating surface is gradually blocked of all samples. To be specific, the diameter of coalesced bubbles on MC-20 and MP-20 samples are even larger than 20.0 mm (third column of Fig. 6), then a giant mushroom-like bubble will block all the heating surfaces to induce the boiling crisis. As a contrast, bare sample (Fig. 6 (a)) and MG-sample (Fig. 6 (b)) have relatively smaller coalesced bubble, and higher CHF is encountered as a result.

3.3. Not all corrosive conditions will deteriorate boiling heat transfer

Fig. 7 (a) shows the CHF variation tendency of SS samples with increasing corrosion time at pH = 8.5, under which condition

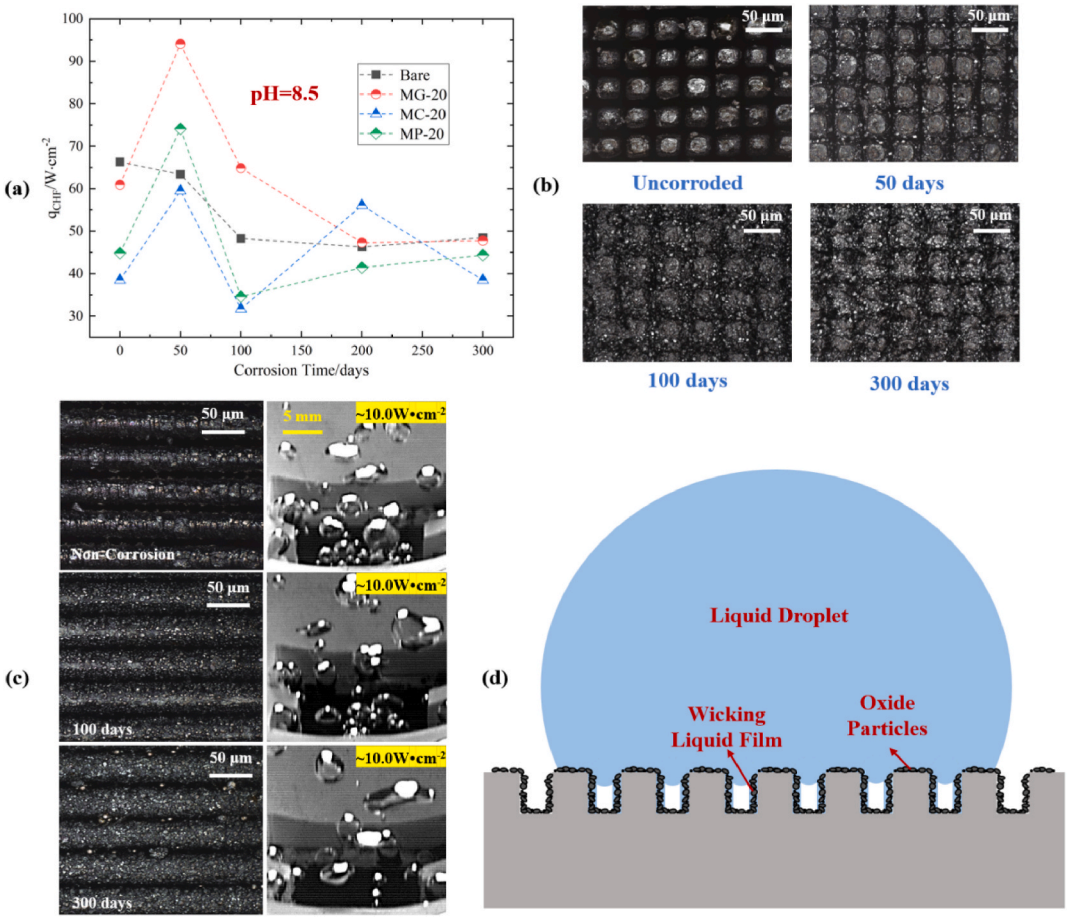

Fig. 7. (a) CHF variation results of SS samples, (b) LSCM images of MP-20 samples, (c) LSCM and visualization images of MG-20 samples, at pH = 8.5 with increasing corrosion time, (d) schematic diagram of wicking liquid film on corroded samples with hierarchical micro/nano structures.

obvious variation trend can be observed. In terms of bare sample, it can be observed that CHF decreases monotonously, from 66.3 to 48.46 W·cm^{-2} as corrosion time increases. Corresponding, CA value gradually increases from original 93.5°–121.6° in 200 days (Fig. S3 (b)). It means that the bare sample gradually becomes more hydrophobic with lower CHF value as a result. This phenomenon also occurs in other article [42] that the CA gradually increases over time when the laser-textured surface is exposed. For instance, the superhydrophilic metal surface after laser texturing is gradually transformed from hydrophilic state into hydrophobic state (~153°) when it is exposed to atmospheric air in 30 days [43]. The main reason is resulted from passive adsorption of hydrophobic VOCs within air and working fluid [22,44]. In order to validate the existence of VOCs on corroded samples, the X-ray photoelectron spectroscopy (XPS) is utilized. As illustrated in Fig. 8, high-resolution spectra of C 1s (AXIS UltraDLD) quantitatively reveals that the content of C–C bonds gradually increases over time, which matches the measurement results of the increasing CA.

As for microstructure samples, the CHF values increase firstly and then decrease. Take MG-20 as an example, it increases from original 60.94 W cm^{-2} to 94.09 W·cm^{-2} in 50 days, then decreases to 47.77 W·cm^{-2} in 300 days and is close to that of bare sample. Fig. 7 (b) depicts the LSCM images of MP-20 samples of different corrosion time, the oxide particles ranging from nanometer to micron formed gradually and attached on the processed microstructure, which alters original surface morphology to a hierarchical micro/nano condition. Based on CHF variation curves in Fig. 7 (a), it is reasonable to assume that proper amount of oxide particles is beneficial to extra wicking liquid supply underneath boiling bubble (Fig. 7 (d)), which can be regarded as the main reason of CHF enhancement at the beginning. After then, too many particles gradually block and fill up the original processed microchannel in 300 days, and its effect on boiling heat transfer is disabled, too. It also can be observed from Fig. 7 (c) that fewer bubbles are generated with longer corrosion time for MG-20 samples, which can result in a relatively lower HTC value. Therewith, surface morphology of SS samples is severely changed by the corrosive environment, and corresponding CHF value and bubble dynamics are both altered as a result.

Fig. 9 (a) shows the cross-section SEM images of SS samples with different corrosion time. It can be observed clearly that the V-shaped microgrooves are gradually blocked and eventually filled up by the formed oxide particles. Long-term corrosion makes the MG sample more or less like a bare sample, and the originally processed microstructure is nearly disabled. The schematic diagram (Fig. 9 (b)) illustrates this complex process more vividly. In order to analyze varying cross-section area quantitatively, binarization processing method (detailed procedures shown in supplementary material S6) can be utilized to calculate corresponding effect on CHF value of microstructure sample in corrosive environment (Fig. 9 (c)).

As aforementioned earlier, Kim et al. [17] analyzed force balance between momentum change due to evaporation and forces acting on bubble, combining with additional capillary force term based on nondimensional average roughness. In this article, a nondimensional number K is applied to consider corrosive effect quantitatively (defined as $\overline{S_c}/S_0$), where $\overline{S_c}$ and S_0 are the actual cross-sectional area of corroded microchannels and original cross-sectional area of uncorroded microchannels, respectively. As the nondimensional average roughness proposed by Kim et al. is proportional to the square toot of nondimensional area, i.e., K, then the revised CHF model can be obtained as depicted in Eq. (11):

$$q''_{CHF,predicted} = S \times \frac{q''_{CHF,Zuber}}{0.131} \frac{1+\cos\beta_f}{16} \left[\frac{2}{\pi} + \frac{\pi}{4}\left(1+\cos\beta_f\right) + \frac{4C\cos\beta_f}{1+\cos\beta_f} K^{1/2}\right]^{1/2} \tag{11}$$

where S and C are the correction factor and constant of proportionality, respectively, and their values are found to be 0.127 and 1135 for the current data set. Fig. 10 shows the comparison results of CHF values between experiment of corroded SS samples and prediction of modified correlation. It can be observed from Fig. 10 that the maximum relative error is only 14.5 % (MG-20-8.5-50d represents that MG-20 sample is corroded at pH = 8.5 for 50 days and the same applies to others), therefore, this modified model based on capillary force of surface roughness can predict actual CHF value of metallic surface with microstructure under corrosive conditions.

In addition, the effect of pH value has also been compared, and the result in Fig. S6 shows it becomes more severe for SS MC-20 samples under corrosive condition (300 days) with increasing pH value, and CHF values basically decrease correspondingly. As a contrast, it can be found in Fig. S7 (b) that CHF values barely change after 100 days corrosion for all Inconel samples, which means that the corrosive environment has little effect on the Inconel samples. Based on LSCM images (Fig. S7 (a)), the surface morphology also has

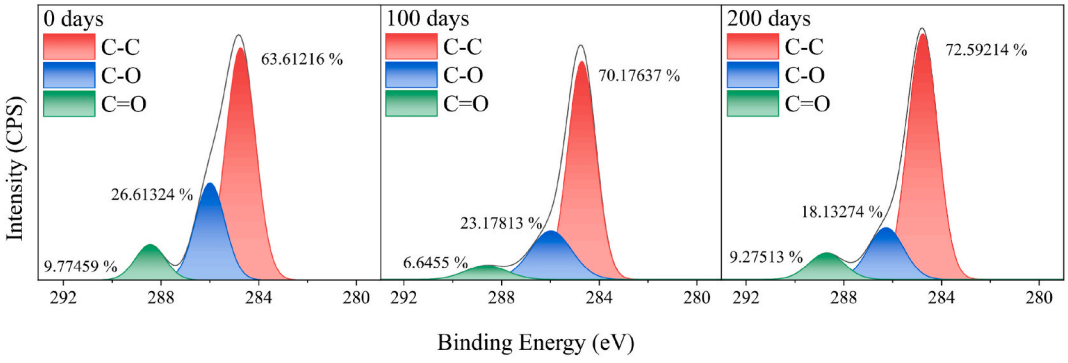

Fig. 8. High-resolution XPS spectra for C 1s of SS samples under 100, 200 days corrosion condition.

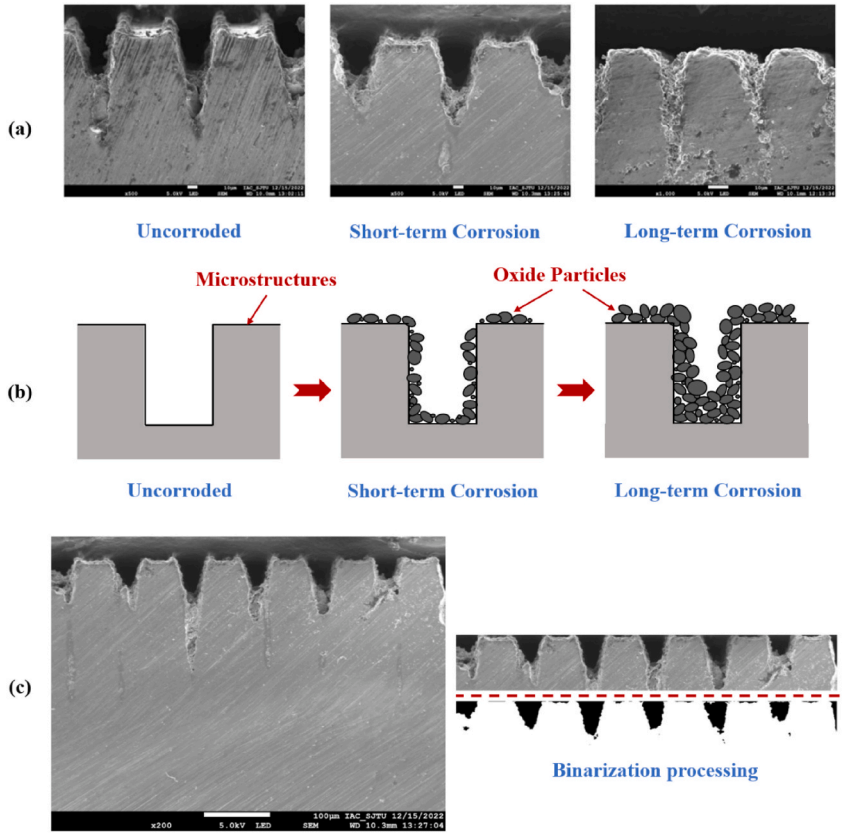

Fig. 9. (a) SEM images, (b) schematic diagram, and (c) quantitative analysis by binarization process method about cross section of SS microgroove samples with different corrosion time.

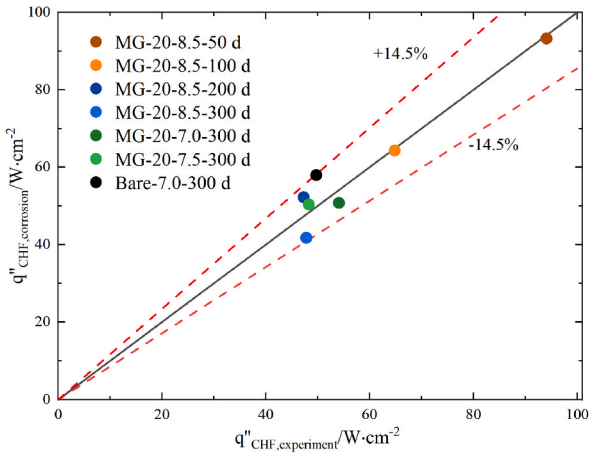

Fig. 10. Comparison results of CHF values between experiment of corroded SS samples and prediction of modified correlation.

changed very little because there are barely no oxide particles formed. Therewith, the widely adopted Inconel material in nuclear industry has very excellent corrosive resistance, its morphology and corresponding boiling heat transfer capability can maintain for such a long time.

4. Conclusions

Comprehensive researches about the corrosive effect on laser processed microstructure samples made of SS and Inconel materials

has been conducted in this article. Different construction and characteristic dimension of microstructure, various duration time and pH value of corrosive environment are compared thoroughly. The key conclusions are obtained as following:

(1) For the uncorroded SS microstructure samples, not all of them can enhance boiling heat transfer characteristics, especially CHF values, which are basically inversely proportional to CA. Besides, CHF values with characteristic dimension 50 μm are usually larger than those with dimension 20 μm, which can be attributed to the easier penetration of water into larger microchannels (more liquid supply).
(2) In terms of corrosive effect on SS samples, CHF values of bare samples decrease monotonously while those of microstructure samples usually increase at first then decrease, and approach to that of bare sample eventually. As a contrast, the CHF values of Inconel samples are nearly constant, which can mainly be attributed to corrosion resistance of different metals.
(3) Both the contact angle and surface morphology can affect the boiling heat transfer behavior, which can also be revealed by the bubble dynamics results. Based on the binarization processing method, the blockage extend of cross section area can be utilized quantitatively to deduce the CHF variation tendency of SS microstructure samples under different corrosive circumstances.

Further, in order to better improve the research, a recommendation for future study is provided as below: A) Due to the limitations of laser processing accuracy, the dimensions of microstructure are irregular (Fig. 9 (a)), which brings difficulties for the quantitative analysis. Hence, precise fabrication methods such as photography and electrochemical deposition are worth considering. B) The characteristic dimensions of the microstructure are set as 20 and 50 μm in this paper, and the CHF of 50 μm samples are larger. More dimension of microstructure samples can be designed for further research to achieve better boiling heat transfer capability. C) The existence of enhancing wicking liquid film due to the formed hierarchical micro/nano structure under corrosive condition needs to be further validated with the help of advanced measurement technology.

Data availability statement

Portion data is already included in the article and supplementary material. Besides, other data will be made available on request.

CRediT authorship contribution statement

Wei Xu: Writing – original draft, Methodology, Conceptualization. **Longchang Tang:** Writing – review & editing. **Ningkang Zhao:** Data curation. **Kun Ouyang:** Validation, Investigation. **Xiaoqiang He:** Project administration. **Xiaojing Liu:** Supervision, Resources.

Declaration of competing interest

The authors declare that they have no known competing financial interests or personal relationships that could have appeared to influence the work reported in this paper.

Acknowledgements

This work was supported by the National Natural Science Foundation of China (Grant Number: 12005133), LingChuang Research Project of China National Nuclear Corporation and Young Elite Scientist Sponsorship Program by CAST. The microscopic characterizations are performed in Instrumental Analysis Center of Shanghai Jiao Tong University. We also would like to thank Dr. Haozhan Su to help preparing the oxidation experiments.

Nomenclature

C_{sf}, n	empirical coefficient
d	distance, m
D_b	bubble diameter, m
h	heat transfer coefficient, W/(m^2·K)
h_{fg}	latent heat, J/kg
k	thermal conductivity, W/(m·K)
q	heat flux, W/m^2
Pr	Prandtl number
R	Radius, m
S, C	correction factor
T	temperature, °C
σ	surface tension, N/m
ρ	density, kg/m^3
ΔT	wall superheat, °C
μ_l	liquid dynamic viscosity, N·s/m^2
β_r	receding angle, °

Subscript

Cu	copper
l	liquid
sat	saturation
v	vapor

Abbreviation

CHF	critical heat flux
CA	contact angle
HTC	heat transfer coefficient
LSCM	laser scanning confocal microscopy
MC	microcavity
MG	microgroove
MP	micropillar
NPP	nuclear power plant
ONB	onset of nucleate boiling
PEEK	polyetheretherketone
RMSE	root mean square error
RPV	reactor pressure vessel
SS	stainless steel
SEM	scanning electron microscope
TC	thermocouple
VOC	volatile organic compounds
XPS	X-ray photoelectron spectroscopy

Appendix A. Supplementary data

Supplementary data to this article can be found online at https://doi.org/10.1016/j.heliyon.2024.e29750.

References

[1] B. Chu, B. Fu, L. Dong, et al., A graphene quantum dot film with a nanoengineered crack-like surface via bubble-induced self-assembly for high-power thermal Energy management applications, Nano Lett. 23 (1) (2022) 259–266, https://doi.org/10.1021/acs.nanolett.2c04254.

[2] J. Li, S. Gao, R. Long, et al., Self-pumped evaporation for ultra-fast water desalination and power generation, Nano Energy 65 (2019) 104059, https://doi.org/10.1016/j.nanoen.2019.104059.

[3] D.E. Kim, D.I. Yu, D.W. Jerng, et al., Review of boiling heat transfer enhancement on micro/nanostructured surfaces, Exp. Therm. Fluid Sci. 66 (2015) 173–196, https://doi.org/10.1016/j.expthermflusci.2015.03.023.

[4] P. Cheng, Z. Tang, X. Chen, et al., Advanced phase change hydrogel integrating metal-organic framework for self-powered thermal management, Nano Energy 105 (2023) 108009, https://doi.org/10.1016/j.nanoen.2022.108009.

[5] T. Gebrael, J. Li, A.R. Gamboa, et al., High-efficiency cooling via the monolithic integration of copper on electronic devices, Nature Electronics 5 (6) (2022) 394–402, https://doi.org/10.1038/s41928-022-00748-4.

[6] A. Schaffrath, A. Wielenberg, R. Kilger, et al., SMRs—overview, international developments, safety features and the GRS simulation chain, Front. Energy 15 (4) (2021) 793–809, https://doi.org/10.1007/s11708-021-0751-2.

[7] Y. Song, C.D. Díaz-Marín, L. Zhang, et al., Three-tier hierarchical structures for extreme pool boiling heat transfer performance, Adv. Mater. 34 (32) (2022) 2200899, https://doi.org/10.1002/adma.202200899.

[8] F. D'Auria, An old issue and a new challenge for nuclear reactor safety, Front. Energy (2021) 1–6, https://doi.org/10.1007/s11708-021-0729-0.

[9] G. Liang, I. Mudawar, Review of pool boiling enhancement by surface modification, Int. J. Heat Mass Tran. 128 (2019) 892–933, https://doi.org/10.1016/j.ijheatmasstransfer.2018.09.026.

[10] W.T. Hsu, D.I. Shim, M.R.S. Yun, et al., Free-standing nanowire printed surfaces with high variability in substrate selection for boiling heat transfer enhancement, Int. J. Heat Mass Tran. 212 (2023) 124313.

[11] L.Y.X. Lum, P.F. Liu, J.Y. Ho, et al., Micro/nanostructuring of metal additively manufactured aluminum alloy for enhanced pool boiling of dielectric fluids, Int. J. Heat Mass Tran. 221 (2024) 125090.

[12] D.E. Kim, S.C. Park, D.I. Yu, et al., Enhanced critical heat flux by capillary driven liquid flow on the well-designed surface, Appl. Phys. Lett. 107 (2) (2015), https://doi.org/10.1063/1.4926971.

[13] S.G. Kandlikar, Enhanced macroconvection mechanism with separate liquid–vapor pathways to improve pool boiling performance, J. Heat Tran. 139 (5) (2017) 051501, https://doi.org/10.1115/1.4035247.

[14] J. Li, G. Zhu, D. Kang, et al., Endoscopic visualization of contact line dynamics during pool boiling on capillary-activated copper microchannels, Adv. Funct. Mater. 31 (4) (2021) 2006249, https://doi.org/10.1002/adfm.202006249.

[15] X.Z. Sun, Q. Li, W.X. Li, et al., Enhanced pool boiling on microstructured surfaces with spatially-controlled mixed wettability, Int. J. Heat Mass Tran. 183 (2022) 122164, https://doi.org/10.1016/j.ijheatmasstransfer.2021.122164.

[16] Y. Song, S. Gong, G. Vaartstra, et al., Microtube surfaces for the simultaneous enhancement of efficiency and critical heat flux during pool boiling, ACS Appl. Mater. Interfaces 13 (10) (2021) 12629–12635, https://doi.org/10.1021/acsami.1c00750.

[17] J. Kim, S. Jun, R. Laksnarain, et al., Effect of surface roughness on pool boiling heat transfer at a heated surface having moderate wettability, Int. J. Heat Mass Tran. 101 (2016) 992–1002, https://doi.org/10.1016/j.ijheatmasstransfer.2016.05.067.

[18] C.M. Kruse, T. Anderson, C. Wilson, et al., Enhanced pool-boiling heat transfer and critical heat flux on femtosecond laser processed stainless steel surfaces, Int. J. Heat Mass Tran. 82 (2015) 109–116, https://doi.org/10.1016/j.ijheatmasstransfer.2014.11.023.

[19] Y. Song, L.N. Zhang, Z. Liu, et al., Effects of airborne hydrocarbon adsorption on pool boiling heat transfer, Appl. Phys. Lett. 116 (2020) 253702.
[20] H.H. Son, U. Jeong, G.H. Seo, et al., Oxidation effect on the pool boiling critical heat flux of the carbon steel substrates, Int. J. Heat Mass Tran. 93 (2016) 1008–1019, https://doi.org/10.1016/j.ijheatmasstransfer.2015.10.047.
[21] K. Wang, N. Erkan, H. Gong, et al., Effects of carbon steel surface oxidation on critical heat flux in downward-face pool boiling, Int. J. Heat Mass Tran. 136 (2019) 470–485, https://doi.org/10.1016/j.ijheatmasstransfer.2019.03.020.
[22] X. Yan, Z. Huang, S. Sett, et al., Atmosphere-mediated superhydrophobicity of rationally designed micro/nanostructured surfaces, ACS Nano 13 (4) (2019) 4160–4173, https://doi.org/10.1021/acsnano.8b09106.
[23] M. Moze, M. Senegacnik, P. Gregorcic, et al., Laser-engineered microcavity surfaces with a nanoscale superhydrophobic coating for extreme boiling performance, ACS Appl. Mater. Interfaces 12 (21) (2020) 24419–24431, https://doi.org/10.1021/acsami.0c01594.
[24] K.L. Murty, I. Charit, An Introduction to Nuclear Materials: Fundamentals and applications[M], John Wiley & Sons, 2013.
[25] I.L. Pioro, W. Rohsenow, S.S. Doerffer, Nucleate pool-boiling heat transfer. I: review of parametric effects of boiling surface, Int. J. Heat Mass Tran. 47 (23) (2004) 5033–5044, https://doi.org/10.1016/j.ijheatmasstransfer.2004.06.019.
[26] J. Kim, J.F. Benton, D. Wisniewski, Pool boiling heat transfer on small heaters: effect of gravity and subcooling, Int. J. Heat Mass Tran. 45 (19) (2002) 3919–3932, https://doi.org/10.1016/S0017-9310(02)00108-4.
[27] R. Wen, S. Xu, Y.C. Lee, et al., Capillary-driven liquid film boiling heat transfer on hybrid mesh wicking structures, Nano Energy 51 (2018) 373–382, https://doi.org/10.1016/j.nanoen.2018.06.063.
[28] W. Xu, K. Ouyang, J. Guo, et al., Experimental and numerical investigations on heat transfer and flow behavior of flow blockage in narrow rectangular channel with protrusions, Appl. Therm. Eng. 203 (2022) 117954, https://doi.org/10.1016/j.applthermaleng.2021.117954.
[29] P.A. Raghupathi, S.G. Kandlikar, Effect of thermophysical properties of the heater substrate on critical heat flux in pool boiling, J. Heat Tran. 139 (11) (2017) 111502, https://doi.org/10.1115/1.4036653.
[30] M.Q. Raza, N. Kumar, R. Raj, Wettability-independent critical heat flux during boiling crisis in foaming solutions, Int. J. Heat Mass Tran. 126 (2018) 567–579, https://doi.org/10.1016/j.ijheatmasstransfer.2018.05.062.
[31] M.M. Rahman, E. Olceroglu, M. McCarthy, Role of wickability on the critical heat flux of structured superhydrophilic surfaces, Langmuir 30 (37) (2014) 11225–11234, https://doi.org/10.1021/la5030923.
[32] A. Gurung, Enhancement of Pool Boiling and Evaporative Heat Transfer Using High Temperature Thermally Conductive Microporous coatings[M], The University of Texas at Arlington, 2014.
[33] A. Ranjan, I. Ahmad, R.K. Gouda, et al., Enhancement of critical heat flux (CHF) in pool boiling with anodized copper surfaces, Int. J. Therm. Sci. 172 (2022) 107338, https://doi.org/10.1016/j.ijthermalsci.2021.107338.
[34] W.M. Rohsenow, A method of correlating heat-transfer data for surface boiling of liquids, Trans. Am. Soc. Mech. Eng. 74 (6) (1952) 969–975, https://doi.org/10.1115/1.4015984.
[35] N. Zuber, On the stability of boiling heat transfer, Trans. Am. Soc. Mech. Eng. 80 (3) (1958) 711–714, https://doi.org/10.1115/1.4012484.
[36] I. Golobič, A.E. Bergles, Effects of heater-side factors on the saturated pool boiling critical heat flux, Exp. Therm. Fluid Sci. 15 (1) (1997) 43–51, https://doi.org/10.1016/S0894-1777(96)00170-7.
[37] P. Griffith, J.D. Wallis, The Role of Surface Conditions in Nucleate boiling[R], Massachusetts Institute of Technology, Division of Industrial Cooperation,[1958], Cambridge, Mass, 1958. http://hdl.handle.net/1721.1/61453.
[38] B. Liu, J. Liu, Y. Zhang, et al., Experimental and theoretical study of pool boiling heat transfer and its CHF mechanism on femtosecond laser processed surfaces, Int. J. Heat Mass Tran. 132 (2019) 259–270, https://doi.org/10.1016/j.ijheatmasstransfer.2018.12.003.
[39] Q.N. Pham, S. Zhang, S. Hao, et al., Boiling heat transfer with a well-ordered microporous architecture, ACS Appl. Mater. Interfaces 12 (16) (2020) 19174–19183, https://doi.org/10.1021/acsami.0c01113.
[40] S.H. Kim, G.C. Lee, J.Y. Kang, et al., Boiling heat transfer and critical heat flux evaluation of the pool boiling on micro structured surface, Int. J. Heat Mass Tran. 91 (2015) 1140–1147, https://doi.org/10.1016/j.ijheatmasstransfer.2015.07.120.
[41] H.J. Cho, D.J. Preston, Y. Zhu, et al., Nanoengineered materials for liquid–vapour phase-change heat transfer, Nat. Rev. Mater. 2 (2) (2016) 1–17, https://doi.org/10.1038/natrevmats.2016.92.
[42] J. Voglar, P. Gregorčič, M. Zupančič, et al., Boiling performance on surfaces with capillary-length-spaced one-and two-dimensional laser-textured patterns, Int. J. Heat Mass Tran. 127 (2018) 1188–1196, https://doi.org/10.1016/j.ijheatmasstransfer.2018.07.056.
[43] P. Gregorčič, B. Šetina-Batič, M. Hočevar, Controlling the stainless steel surface wettability by nanosecond direct laser texturing at high fluences, Appl. Phys. A 123 (2017) 1–8, https://doi.org/10.1007/s00339-017-1392-5.
[44] J. Li, Y. Zhao, J. Ma, et al., Superior antidegeneration hierarchical nanoengineered wicking surfaces for boiling enhancement, Adv. Funct. Mater. 32 (8) (2022) 2108836, https://doi.org/10.1002/adfm.202108836.